

pubs.acs.org/JPCC Article

Excitons in Hematite Fe₂O₃: Short-Time Dynamics from TD-DFT and Non-Adiabatic Dynamics Theories

Lili Rassouli, Mohammad Shakiba, Alexey V. Akimov, Xuyan Ma, and Michel Dupuis*



Cite This: J. Phys. Chem. C 2024, 128, 13681-13693



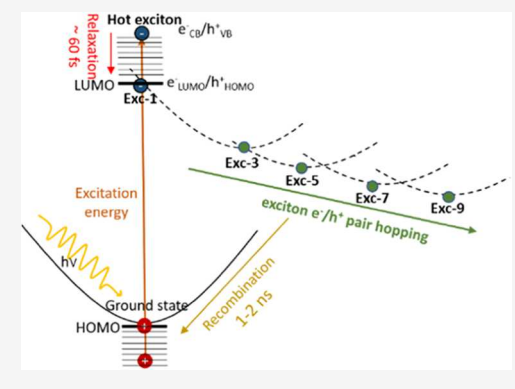
ACCESS I

III Metrics & More

Article Recommendations

Supporting Information

ABSTRACT: We present a first-principles study of the short-time dynamics of excitons in hematite Fe_2O_3 . We used time-dependent density functional theory (TD-DFT) with an underlying DFT+U treatment of electron interactions to characterize the electronic structure of excitons and nonadiabatic molecular dynamics theory (NA-MD) to determine their recombination (electronic ground-state recovery) and relaxation dynamics. Decoherence-corrected trajectory surface hopping approaches in NA-MD simulations yielded recovery times of \sim 1.1 to 1.8 ns and "higher-lying" exciton relaxation times of \sim 60 to 70 fs, in accord with experimentally derived lifetimes. With hematite phonons in the range of \sim 100 to 700 cm⁻¹, higher-lying excitons relax within one or two oscillations of the phonons before getting trapped into an electron—hole pair Exc-3 structure on the first excited state potential energy surface. This structure resembles already a pair of polarons (electron polaron plus hole polaron) with associated lattice



distortions three (3) basal planes away. On longer time scales, the electron—hole bipolaronic pair hops to structures Exc-5, then Exc-7, then Exc-9, ... with the electron polaron and hole polaron separated by 5, 7, 9, ... basal planes in a process of charge separation. The largest frequency phonon \sim 672 cm⁻¹ for the Exc-3 exciton structure is associated with the electron polaron moiety of the exciton. This phonon is a good candidate for giving rise to the recently observed and reported postexcitation transient IR absorption peak.

I. INTRODUCTION

Concerns about environmental problems have motivated society to turn to green energies as sources of fuel, particularly solar energy. The science underlying photoelectrochemical devices (PECs) revolves around charge carriers: (a) light absorption and charge carrier generation (electrons and holes), (b) charge carrier separation and transport, and (c) charge carrier utilization in interfacial redox reactions that leads to solar fuels.^{2,3} Characterization, understanding, and controlling the structure and dynamics of charge carriers are essential to design systems and devices with enhanced photoelectrochemical conversion efficiencies. 4-6 Computational contributions to this end may include characterization of the optical absorption of the structure and dynamics of electron-hole pair excitons (relaxation and recombination-ground state recovery), and of their separation into electron and hole polaron charge carriers in candidate electrode materials, for example transition metalbased semiconductors as studied here.⁶

The present study deals with hematite Fe_2O_3 as a photoactive semiconductor oxide, attractive for PECs and often used as a model system for experimental and computational investigations. Its attractiveness arises from its abundance, its stability, and its narrow band gap that enables absorption of visible light.^{7,8} Fe_2O_3 falls in the class of materials in which electrons exhibit strong correlation and the d electrons in the Fe 3d atomic-like states are high-spin coupled

within basal planes and antiferromagnetically coupled across basal planes.

The initial impetus for the present research was the work from Biswas et al.,9 which examined the structure of photogenerated excitons through XUV experimental characterization. These authors reported that electron-hole pair excitons in hematite (and several other oxides) arise from ligand-to-metal excitations and that exciton radii are of the order of a single metal-oxide bond. In the first paper of this series 10 (Paper I), we reported the computational characterization of the nature of excitons and electronic excited states in hematite.¹⁰ In particular, we identified excitonic structures that resemble electron polaron-hole polaron pairs separated by 3, 5, 7, 9, ... basal planes. We referred to them as Exc-3, Exc-5, Exc-7, and Exc-9 structures and described them as precursors to separated electron polarons and hole polarons. Figure 1 summarizes the findings from Paper I, albeit it incorporates new computational results presented in the present work.

Received: May 16, 2024 Revised: July 18, 2024 Accepted: July 29, 2024 Published: August 9, 2024





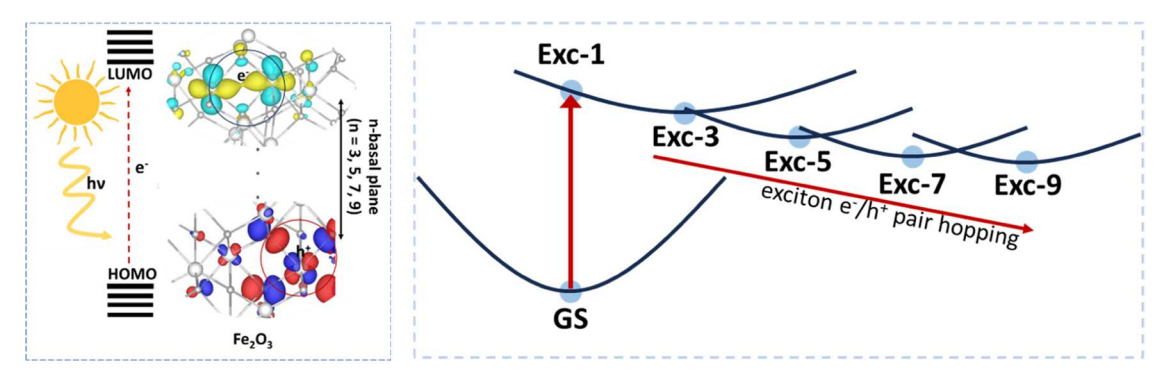


Figure 1. Excitons in Fe₂O₃. The left panel depicts the structures of electron polaron—hole polaron pairs as excitons. HOMO and LUMO refer to the one-particle state of an electron/hole pair exciton. The right panel illustrates the potential energy surface of the lowest-lying exciton. GS = ground state, Exc-1 = vertical low-lying exciton, Exc-3,5,7,9 = electron polaron—hole polaron separated pairs.

In the present work, we characterize the early time dynamics of these excitons, including their kinetics of nonradiative relaxation, and the nature of the first excited state potential energy surface (PES) governing the kinetics. To this end, we used the theories of time-dependent density function theory (TD-DFT) and nonadiabatic molecular dynamics (NA-MD).

I.I. Exciton Dynamics and Time Scales. To set the context of the present research, it is useful to refer to the review by Corby et al.¹¹ Under sunlight irradiation, excitation occurs that creates excitons (electron-hole pairs) with a range of energies, from the lowest energy exciton to higher energy excitons. Higher-lying excitons undergo nonadiabatic transitions across the ladder of excited states or recombination transitions to the ground state. During relaxation, the electron from the excitonic electron-hole pair can be described as relaxing down to the conduction band edge (LUMO) with the hole relaxing up to the valence band edge (HOMO). Exciton relaxation in hematite and similar metal oxide semiconductors occurs on the time scale of femtoseconds to picoseconds. 11,12 Exciton separation occurs when excitonic electrons and holes self-trap into electron and hole polarons far away from each other on the time scale of pico- to nanoseconds. 11 Prior to exciton relaxation and electron-hole separation, the electron may recombine with the hole into an electron pair of the ground state wave function. In semiconductors with a large band gap, recombination occurs on the time scale of pico- to nanoseconds. 11 In photocatalysis, the separated self-trapped polarons, also referred to as "charge carriers", migrate from the bulk to the surface where they participate in oxidation or reduction reactions, such as water oxidation or proton reduction, and other reactions. Carrier transport occurs on the time scale of micro- to milliseconds, with surface redox reactions on a time scale of up to seconds.¹¹

A recent characterization of the structure of excitons at the length scale of bonds and of exciton radii in selected metal oxides⁹ spurred our earlier work on the structure of excitons in hematite via first-principles computation.¹⁰ Here we are interested in characterizing and understanding the early time dynamics of photogenerated excitons in Fe₂O₃, in determination of the relaxation and recombination times for "higherlying" excitons, and in describing the potential energy surface of the lowest energy exciton state whereby the relaxed "higherlying" excitons convert to charge-separated (electron polaron—hole polaron) pairs (Exc-3 in Figure 1) as onset of charge separation and generation of separated electron polarons and hole polarons.

I.II. Relevant Prior Experimental and Computational Studies. Several experimental and computational studies of hematite can be found using X-ray absorption spectroscopy (XAS), ¹³ resonant inelastic X-ray scattering (RIXS), ¹⁴ extreme ultraviolet spectroscopy (XUV), 15 and other studies. Carneiro et al. 16 coupled extreme ultraviolet (XUV) and optical absorption to assign the spectroscopic features to small polaron formation within ~100 fs after photoexcitation, with the fastest formation rate for visible light absorption of ~2.5 eV. The authors also stated that the data is not consistent with the occupation of a midgap or surface state with lifetime. Figure 1 that emerged from our prior work¹⁰ and the present study is consistent with these statements. The same authors also stated unequivocally that visible light absorption has O 2p to Fe 3d character, even when allowing for hybridization of these atomic states. Biswas et al. 9,15,17 reported bulk polaron formation within ~90 fs based on XUV data combined with reflection-absorption, with surface polaron formation significantly slower. 15,17,18 Probing the M edge of the Fe species and the L edge of the O species also revealed the O 2p to Fe 3d character of low-energy excitons. Furthermore, this approach led the authors to extract an exciton radius of one (1) M-O bond. This characterization of exciton radius in several oxides prompted our earlier work 10 and the present one. Ismail et al. 19 used ultrafast X-ray absorption spectroscopy (XAS) and resonant inelastic X-ray scattering (RIXS) measurements and reported findings consistent with an earlier assignment by Vura-Weis et al.²⁰ of the ligand-to-metal O 2p to Fe 3d nature of the optical excitation. These authors reported relaxation of higher-lying electrons within ∼1 ps, fast carrier recombination to the ground state within ~10 ps, and evidence for long-lived trapped electron states (with lifetimes of the order of ~ hundreds of picoseconds). Similar time scales were reported by Joly et al.²¹ based on transient reflectivity measurements. Relevant to the present work are the postexcitation transient IR spectroscopy measurements carried out by Suligoj et al.²² These authors reported the appearance of a peak at \sim 640 cm⁻¹ with a lifetime considerably longer than carriers lifetimes in hematite. We will show below that the transient exciton structure Exc-3 depicted in Figure 1 exhibits a distinctive vibration, calculated at ~672 cm⁻¹ and localized on the electron state side of the exciton. As we describe the Exc-3 structure as a precursor of the separated electron and hole polarons, we suggest that the observed postexcitation transient IR peak may correspond to the signature vibration of electron polarons.

On the computation and simulation side, Fe₂O₃ is generally viewed as challenging because of its complex electronic structure and the strong electron correlation. Several methods have been used to study the excitation spectrum of hematite. Among those, the GW-BSE method is based on quasi-particle theory. As seen in Piccinin et al.²³ and in Snir and Toroker,²⁴ GW-BSE treatments have challenges in accurately predicting the band gap and the optical spectrum. Another notable study is the one by Ahart et al. 25 These authors were the first to suggest, based on hybrid DFT calculations, that isolated electron polarons in hematite are "localized" over two Fe atoms belonging to edge-sharing octahedra. The assertion was supported by Shelton and Knowles^{26,27} in their DFT+U calculations of electron-phonon couplings in Fe₂O₃, albeit these authors favored the widely accepted O 2p to Fe 3d description of the optical absorption in Fe₂O₃. These authors also identified two phonons distinctly associated with the electron polaron at 250 and 653 cm⁻¹. Our earlier work¹⁰ based on TD-DFT calculations combined with spin-polarized DFT+U revealed that, in fact, the electron state of an exciton also exhibits the localized-over-two-Fe character, as depicted in Figure 1, with the hole state having a strong O 2p character spread over the O atoms of a FeO₆⁺ moiety. Cheng et al.²⁸ used hybrid DFT theory combined with the Δ SCF-based description of excited states and NA-MD theory that yielded recombination times of ~110 ps in hematite. Lastly, we note the derivation by Klein et al.²⁹ of a formalism that enables to identify the factors that contribute to XUV spectra, including accounting for the short-time trapping of polarons. However, their approach does not seem to provide information about time scales.

Our objective in a series of studies was to cross-validate advanced chemical theories and experiments at the length and time scales of chemical bonds for strongly correlated systems. Paper I dealt with the electronic structure and polaronic structures of electron-hole pair excitons in hematite, highlighted in Figure 1.10 Here (Paper II), we address the shorttime dynamics of these excitons, investigated through the characterization of the shape of the excited state potential energy surface upon vertical excitation, and the determination of excited state relaxation and recombination (ground state recovery) times. The former is carried out using TD-DFT theory, as in Paper I, and the latter using NA-MD theory. The paper is organized as follows: in Section II, we outline the TD-DFT and NA-MD protocols and some aspects of phonon analysis; in Section III, we present the results, addressing the dynamics and the shape of the 1st-Ex potential energy surface, leading to Figure 1. We conclude in Section IV.

II. METHODS

II.I. Electronic Structure Computations. For details and results about the spin-polarized DFT+U and TD-DFT protocols used throughout this work, we refer the reader to Paper I. There, we determined the ground state optimized structure (GS) on the DFT potential energy surface using a 2 \times 2 \times 1 supercell. We also reported the optimized geometry of the TD-DFT first excited (lowest excitation energy) state (1st-Ex). The resulting local minimum energy structure was the structure denoted Exc-3, with a "localized" electron state of Fe 3d character (shared by two Fe atoms that are centers of two edge-sharing octahedra), a "localized" hole state of O 2p character spread over an FeO₆+ octahedron, and the two sites separated by 3 basal planes, depicted in Figure 1 above.

In this work, the nature of the GS structure as an energy minimum was established by calculating the Hessian matrix of the GS state, which showed all positive vibrational frequencies. The 1st-Ex state at the optimized GS geometry is neither a minimum nor a transition state, as it has a nonzero gradient. Several points on the steepest descent path for the 1st-Ex state starting at the GS structure as well as the energy profile of the 1st-Ex state along a linearized pathway that morphs the GS structure and the Exc-3, are discussed in this work. The findings led us to the picture shown in Figure 1 above, with the vertical excitation reaching a side of the Exc-3 energy well.

II.II. Phonons Analysis. Figure 1 illustrates the electronic structure of the excitonic local minima Exc-3, Exc-5, Exc-7, and Exc-9 on the state potential energy surface of the first excited state as established in Paper I. We described them broadly as electron polaron—hole polaron pairs owing to the localized nature of the electron and hole states of the excitonic electron—hole pair. They exhibit lattice distortions typical of polarons with bond length changes notable for several bonds associated with the polaronic centers. Considering these structural changes, we are interested in identifying phonons that could be viewed as signatures of the electron polaron and hole polarons, with potential comparison with the results from Shelton and Knowles. 26,27

To identify these localized phonons (vibrational modes), we used the Generalized Subsystem Vibrational Analysis (GSVA) method of Tao et al.³⁰ The method uses the dynamical matrix of a full system and associated "full" normal modes of vibration (phonons) and defines a back transformation to project out the dynamical matrix of a specific subsystem. The subsystem is chosen to be the smaller excised cluster of atoms that exhibit the lattice distortion of the excitons or polarons. We apply a projection of the subsystem modes onto the full system modes by calculating the cosine of the angles of projection between the subsystem modes and the full system modes. This enables us to identify the full system modes that resemble most the easy-to-identify subsystem modes. We will remark that the projection is determined between the modes expressed in mass-weighted Cartesian coordinates rather than the modes expressed in conventional Cartesian coordinates. Indeed, in mass-weighted Cartesian coordinates, the full system modes form an orthonormal basis of modes (displacements), so that the dot product between subsystem modes and full system modes is a rigorously defined measure of similarity. In Paper I, 10 we described the electron polaron site as exhibiting a shortening of the Fe-Fe bond between the Fe centers of two edge-sharing octahedra. The hole polaron site exhibits the shortening of Fe–O bonds in a FeO₆⁺ subunit. The subsystems of interest are then the two edge-sharing octahedra for the electron polaron site (excised 12 atom cluster denoted as 12cluster) and one octahedron FeO₆⁺ unit for the hole polaron site (excised 7 atom cluster denoted as 7-cluster), independently or together. Among the Fe-O bonds of the 12-cluster, only two exhibit significant shortening, they are the bonds most aligned with the Fe-Fe bond, seen in Figure S1 in SI, and we refer to these atoms as the 4-cluster with a O-Fe-Fe-O linkage. Among the six Fe-O bonds of the hole site, only the four equatorial Fe-O bonds show significant shortening. We select them as a 5-cluster.

To characterize the first excited state potential energy surface near the GS structure (vertical excitation), we also used a vibration analysis whereby we selected a modified orthonormal basis (rather than a Cartesian coordinate basis) of displacements to perform the analysis. In one case, we took the structure change (normalized) vector $DX(i) = X_{\text{Exc-3}}(i)$ – $X_{GS}(i)$, (i = 1,...,3N) between the GS and Exc-3 structures and supplemented it with a Gram-Schmidt basis of order 3N-1. We refer to DX as the "Marcus" pathway, which is often used to characterize polaron hopping. In another case, we selected the gradient direction vector of the 1st-Ex state at the GS geometry supplemented with a Gram-Schmidt basis. This gradient vector defines the steepest descent path that one might use to locate the minimum energy structure of the first excited state upon vertical excitation. These modified analyzes enable us to quantify the harmonic frequencies along these selected 1D directions on the Exc-3 or GS potential energy surfaces. If we denote B the $3N \times 3N$ matrix of the modified displacement basis (analogously to when using internal coordinates), the vibrational eigenproblem involves the force matrix $F = B^{-1}$ $M^{-1/2}$ H $M^{-1/2}$ B rather than the usual force matrix $F = M^{-1/2}$ $H M^{-1/2}$, where M is the diagonal matrix of atomic masses and H is the Hessian matrix of energy second derivatives.

II.III. DFT+U, Functional, Basis Sets, and Supercell. We used DFT^{31,32} with the Perdew–Burke–Ernzerhof (PBE) exchange-correlation functional³³ for the description of the ground state wave function of $Fe_2O_3^{34}$ augmented with Hubbard +U³⁵ one-center terms on Fe atoms and on O atoms as corrective treatment for the self-interaction error of DFT. An extensive comparison with hybrid functionals and various values of +U(Fe) and +U(O) corrections resulted in the selection of +U(Fe) = 3.0 and +U(O) = 2.0 as a good choice of parameters yielding good structure and HOMO–LUMO band gap ~2.09 eV for a 2 × 2 × 1 supercell and for minority spin electrons in accord with experimental values of ~2.0 to 2.2 eV.³⁶ The use of +U on O atoms was deemed important when considering the possibility of creating a hole with an unpaired spin on O atoms upon excitation.¹⁰

We used the DZVP-MOLOPT-SR-GTH basis set for the valence electrons of Fe and O atoms³⁷ and employed the GTH-PBE pseudopotentials to describe the core electrons.³⁸ The DZVP-MOLOPT-SR-GTH basis set is a 'double- ζ plus polarization' basis set. Accordingly, it provides a qualitatively reliable description of the Mulliken atomic populations of the Fe and O atoms. We believe that differences in Mulliken populations between the polaronic vs bulk centers are chemically meaningful when describing the excited states and their associated localized lattice distortions. Through tests on the band gap, we limited ourselves to Γ point sampling of the Brillouin zone and settled on using a $2 \times 2 \times 1$ supercell as sufficient to describe qualitatively correctly the ground state structure GS and the exciton structure Exc-3 with the electron and hole sites separated by three basal planes. Extensive details are provided in Paper I. The $2 \times 2 \times 1$ supercell consists of 120 atoms, including 48 Fe atoms and 72 oxygen atoms, and 600 occupied α states and 600 β states. Hematite exhibits FeO₆ octahedra with iron (Fe) atoms surrounded by six oxygen (O) atoms. The octahedra have two sets of three Fe-O bond lengths. Cell parameters optimized at this level of theory are a = b = 5.033 Å and c = 13.74 Å, $\alpha = 90.0^{\circ} \beta =$ 90.0°, and $\gamma = 120.00^{\circ}$ with Fe–O bond lengths of ~1.94 and 2.12 Å in the optimized geometry of the ground state, in good accord with experiment. 39,40 The Mulliken spin moments at the GS geometry with this PBE+U(Fe, O) level of theory are $\sim \pm 4.18$ for Fe atoms, a clear indication of high spin Fe layers and antiferromagnetic coupling across bilayers.

The projected density of state indicates that a minority spin electron β can be excited into iron atoms that have formally no β electrons in the Fe 3d atomic states (Fe $_{\alpha}$ basal planes that lie 1, 3, 5, 7, 9 basal planes away from the hole O atoms). Indeed, the Mulliken analysis indicates that Fe 3d atomic states contribute predominantly to the lowest unoccupied molecular orbital (LUMO), while the O 2p atomic states dominate the contributions to the highest occupied molecular orbital (HOMO).

II.IV. TD-DFT. We used the linear response TD-DFT method embodied in the CP2K suite of programs. ⁴¹ TD-DFT is a single excitation theory. The excited states are linear combinations of singly excited determinants generated by excitations of one electron from any occupied Kohn–Sham (KS) state to any unoccupied KS state. Details of selected calculations can be found in Paper I. ¹⁰

II.V. Molecular Dynamics Simulation. We carried out phase space sampling via a molecular dynamics (MD) simulation within the canonical ensemble of constant temperature of 300 K starting from the optimized structure of the ground state using a canonical ensemble through velocity rescaling thermostat. The time step was taken as 1 fs, and the simulation length was 6.1 ps. We observed that thermalization was achieved within ~1.8 ps. Accordingly, we discarded the first 1800 MD steps from phase space averaging and carried out the NA-MD stochastic simulations of recombination and relaxation over the remaining 4300 MD steps. We demonstrate below that phase space sampling remains in the region of the ground state and does not reach into the region of the Exc-3 state, owing to the large lattice distortion.

II.VI. Nonadiabatic Molecular Dynamics NA-MD Theory. For the NA-MD investigation, we employed the Libra software (version 5.3.0), 43-46 coupled with the CP2K program (version 2022.1), 41,47 to characterize the quantum dynamics of the excitons. The NA-MD protocol encompassed the TD-DFT descriptions of excited states combined with the fewest switches surface hopping (FSSH) algorithm⁴⁸ to describe excited state transitions. To account for electronic structure decoherence, we used the modified simplified decay of mixing (mSDM)^{49,50} and instantaneous decoherence at attempted hops (ID-A)⁵¹ algorithms. A more detailed description of the algorithms and tools can be found elsewhere. 46,52 The overall protocol involves 4 steps: (1) constant temperature molecular dynamics of the system in its ground state to sample phase space using CP2K; (2) identification of diabatic excited states along the molecular dynamics trajectory (MD) using Libra/CP2K because of a challenge due to the closeness of the excited states; (3) determination of the nonadiabatic electronic coupling (NAC) terms along the MD trajectory using Libra; (4) stochastic dynamics simulations, including surface hopping⁴⁸ among the excited states (and possibly including the ground state) to extract recombination (ground state recovery) and relaxation times using Libra.

Calculating the evolution of nuclei in response to changing electronic states is the primary goal of the NA-MD approach in Libra. The electron—nuclear wave function follows eq 1, where $[\psi_i(r;R(t))]$ is the basis set of electronic states. NA-MD is based on the neglect-of-back-reaction approximation (NBRA) of Prezhdo and co-workers combined with the many-body (MB) treatment of the electronic states (here, via TD-DFT). Calculating the evolution of nuclei in response to changing electronic states is computationally expensive in

condensed matter systems; NA-MD uses NBRA to evolve nuclei based on state-independent forces.

$$\psi(r, t; R(t)) = \sum_{i=1}^{N} c_i(t) \psi_i(r; R(t))$$
(1)

The time evolution of the wave function follows the timedependent Schrodinger equation as in eq 2

$$i\hbar \frac{\partial \psi(r, R, t)}{\partial t} = \hat{H}(r, R, t)\psi(r, R, t)$$
(2)

The simplified version of eq 2 has the following form

$$i\hbar \frac{\partial c_i}{\partial t} = \sum_{j=1}^N H_{ij}^{vib} c_j \tag{3}$$

where the vibronic Hamiltonian equation is $H^{vib}_{ij}=H^{-ihd_{ij}}_{ij}$. In this equation, H_{ij} is the electronic Hamiltonian matrix elements, d_{ij} is the nonadiabatic coupling element between states i and j and calculated as $d_{ij}=\langle \phi_i | \frac{\partial}{\partial i} | \phi_j \rangle$, computed numerically using Hammes–Schiffer–Tully (HST) finite difference formula. The coherent amplitude of c_i is then utilized to calculate the surface hopping probabilities of eq 4 that enter Tully's FSSH approach

$$P_{i\to j}(t) = \frac{2d_{ij}c_i(t)c_j^*(t)}{|c_i(t)|^2} dt$$
(4)

In trajectory surface hopping nonadiabatic dynamics, nuclei evolve according to classical Newtonian equations of motion. The trajectory may evolve on a single PES or may change to another one stochastically with the calculated probabilities. During excitation and relaxation, the electronic states change, but the NBRA neglects the effect of new electronic states (electronic state transitions) on nuclear evolution. We used the two surface hopping approaches that capture the decoherence mechanisms: ^{57,58} (1) the ID-A algorithm and (2) the mSDM algorithm which builds upon the original SDM method. Correcting decoherence is important as electronic coherence is lost through interactions with nuclei or the surrounding environment. ⁵⁹ Both approaches are based on the NBRA-FSSH algorithm with coherent amplitude modification. In ID-A, the coherent amplitude is modified at every attempted hop, while in mSDM, it is modified at every time step. ⁴⁶

II.VI.I. NA-MD Simulations. We determined 50 excited states for each point on the MD trajectory. The energy range among these 50 states is \sim 0.2 eV above the first excited state. We carried out stochastic NA-MD simulations for states 1, 5, 10, 20, 30, 40, and 50 as the initial excited states. We performed NA-MD simulations over 21 initial conditions, and for each of these initial conditions, we carry out 500 stochastic realizations of surface hopping simulations. The process was repeated 10 times (10 batches in Libra's terminology) with different seeds for the random number generator. All in all, we carried out a total of $21 \times 10 = 210$ stochastic simulations, each 4000 fs long. For relaxation lifetimes, we included all 210 curves in the fitting process. For recombination lifetimes, we averaged the 10 batches carried out and used 21 curves in the fitting.

The excited states provided by TD-DFT are ordered by energy from lower to higher excitation energy. Because of the very small energy gaps among the excited states, there is a high likelihood that the excited states may change in electronic structure character. To construct a set of states with consistent electronic structure characteristics from the adiabatic TD-DFT states, a state reordering mapping was employed prior to carrying out the NA-MD stochastic simulations. 45,60,61

For the characterization of the recombination lifetime, we included all 50 excited states and the ground state in the NA-MD dynamics and utilized the populations of the ground state to extract the recombination lifetime. To extract recombination times, we employed an exponential function of the form in eq 5

$$p(t; E_0) = 1 - \exp\left(-\left(\frac{t}{\tau}\right)^{\beta}\right) \tag{5}$$

The fits with $R^2>0.8$ were selected for calculating the average lifetime. To evaluate the uncertainty in recombination time calculations, we employed the standard error-bar calculation method, where the error is given by $\varepsilon=Z\frac{\sigma}{\sqrt{n}}$ equation, where n is the number of fitted curves with specific R^2 and σ is the standard deviation of data. The standard normal deviation Z in the error-bar calculation depends on the sample size n. For instance, for sample sizes greater than 120 (n>120), Z is set to 1.960, and for sample sizes of 10 (n=10), Z is set to 2.228. 62

For the relaxation lifetime, we included the 50 excited states in the NA-MD dynamics and used the populations of the low excited state(s) as the "relaxed" state. However, given the small energy range among the low-lying excited states, we defined an energy range (window) of 0.03 eV relative to the first excited state to declare that 'relaxation' had been reached. A challenge arises in extracting relaxation time because of the shape of the curves "population vs time". As will be seen below for the state population curves for the 50th excited state, the plot shows a very rapid decay followed by a plateau of fluctuations. Accordingly, using a modified fitting function was deemed appropriate, as in eq 6.

$$f(t, E_0, B) = (E_0 - B) \exp\left(-\left(\frac{t}{\tau_1}\right)^2\right) + B$$
 (6)

III. RESULTS AND DISCUSSION

III.I. UV—vis Spectrum. TD-DFT indicated that the low energy UV—vis spectrum of hematite is the result of excitations from the valence band of O 2p states to the conduction band of Fe 3d states. The excited state spectrum for the 50 low-lying states at the GS geometry is shown in Figure 2. This figure shows that these excited states have very close energies, within a range of approximately 2.5 nm (\sim 0.01 eV), with some higher states exhibiting larger oscillator strengths.

III.II. Excited State Energies and NACs. The time evolutions of the energies of six selected excited states among the 50 calculated excited states along the MD trajectory are shown in Figure 3. These excited state energies are within a range of 0.2 eV and remain very close throughout the MD (very small spacing), resulting in large NACs among the excited states, as seen in the color map ⁴⁵ in Figure 4. In Figure 4, the largest couplings are shown in yellow, highlighting strong interactions of ~20 meV between excited states and their nearest states. In contrast, NACs between excited states and the ground state are in black, close to ~0 meV. The high

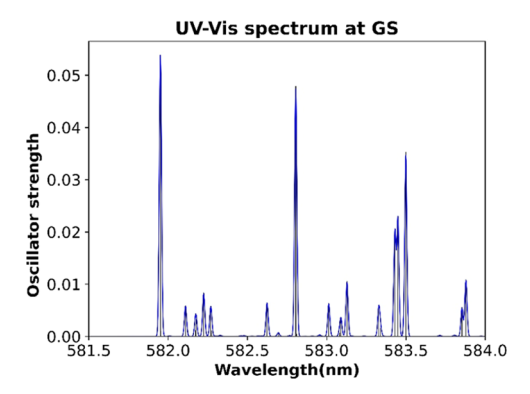


Figure 2. UV—vis spectrum at GS geometry from TD-DFT with DFT +U(Fe,O). See Paper I. (ref 10).

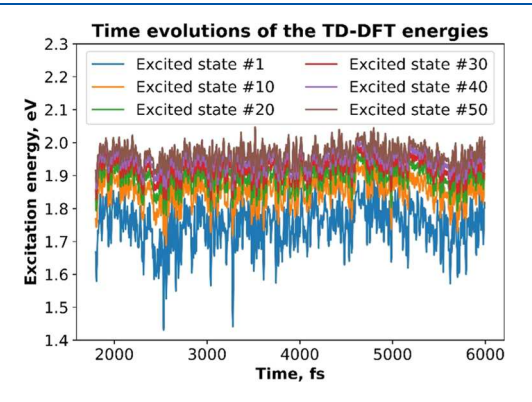


Figure 3. Time evolutions of the TD-DFT energies for selected states along the MD trajectory.

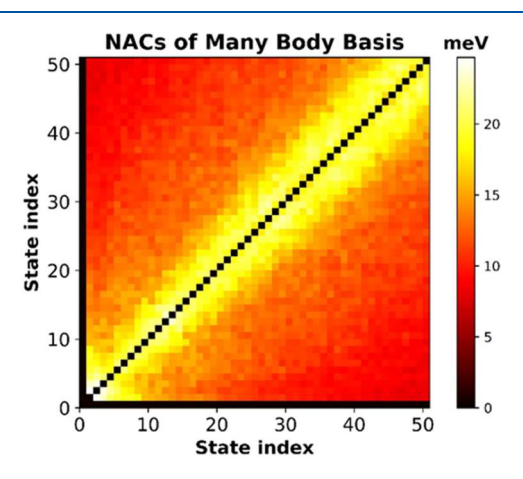


Figure 4. Time-averaged NACs in meV among the 50 excited states and ground state and their associated color scale.

density of the excited states has implications when it comes to identifying the diabatic states during the NA-MD procedure.

An important point must be made as we consider Figures 3 and 1 of this paper and Figure 1 in Paper I where we quantified the energy profile via TD-DFT calculations. The vertical excitation for the 1st-Ex state is \sim 2.12 eV. Upon geometry optimization of the 1st-Ex state, the *lattice distortion energy* for the GS ground state amounts to \sim 0.76 eV (in a 2 \times 2 \times 1 supercell), with an 1st-Ex excitation energy of \sim 1.04 eV at the 1st-Ex optimized geometry, corresponding to an energy relaxation for the 1st-Ex state of \sim 0.32 eV when going from the GS structure to the 1st-Ex structure. As illustrated in Figure 3, the excitation energies of the MD states do not come close

to the value of ~ 1.04 eV, which is the lowest excitation energy at the 1st-Ex state optimized geometry. Accordingly, it can be said that the equilibrated MD trajectory does not sample phase space in the vicinity of the 1st-Ex state structure, also labeled at Exc-3 in Figure 1 above. The only access to the Exc-3 structure is via photoexcitation. As further indication that phase space sampling in MD does not reach into the 1st-Ex (Exc-3) region, we plotted the fluctuations of key bond lengths during the MD simulation. The key bonds are the ones in Exc-3 that show notable differences from the GS structure. For example, we identified in Paper I one Fe-Fe "bond" and four (4) Fe-O bonds that are signatures of the electron state polaron and hole state polaron of the exciton. We fitted the fluctuations with a straight line, plotted a straight line corresponding to the GS optimized value, and plotted a straight line corresponding to the optimized value in the Exc-3 structure. The data is shown in Figure 5 for the Fe-Fe "bond" between the two centers

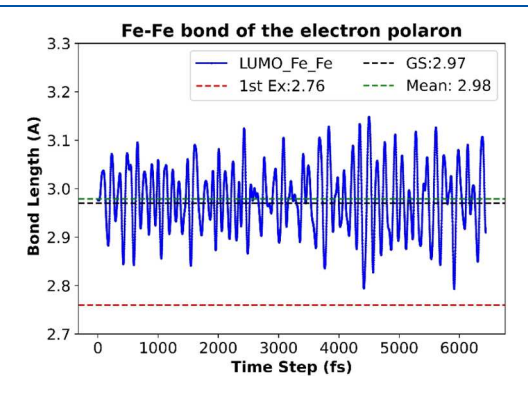


Figure 5. Fluctuations of the Fe—Fe "bond" of the electron polaron site along the MD trajectory. Also shown are a straight line fitting of the fluctuations and straight lines corresponding to the optimized values of the "bond" in the GS and 1st-Ex (Exc-3) geometries. The MD phase sampling around the GS structure does not reach into the region near the Exc-3 structure.

involved with the electron polaron site in Exc-3. The data for the four (4) significant Fe—O bonds of the hole site are given in Figure S2 in the SI file. These plots support the observation that the MD fluctuations do not sample phase space near Exc-3.

The nonadiabatic coupling coefficients between excited states were calculated based on many-body (MB) treatment of excited states (TD-DFT in the present case) rather than single particle (SP) treatment as done in some and past studies. 63,6 The MB approach provides a more accurate treatment of excited states because the SP approach neglects the interaction between electronic states and relies on the properties of oneelectron molecular Kohn-Sham orbitals to calculate state energies and NACs. In contrast, the MB approach gives for each excited state a linear combination of single-particle excitations with optimized coefficients obtained from the linear response equations, thus providing a better representation of excited states. The average magnitudes of the NACs for the ground state and excited state, shown by the black areas in Figure 4, are close to zero. For instance, the magnitudes of the NACs between the ground state and the first, 10th, 20th, 30th, 40th, and 50th excited states are 0.37, 0.33, 0.32, 0.30, 0.30, and 0.29 meV respectively. This observation indicates small coupling between the ground state and the excited states, as is often the case for large band gap systems. In contrast to the

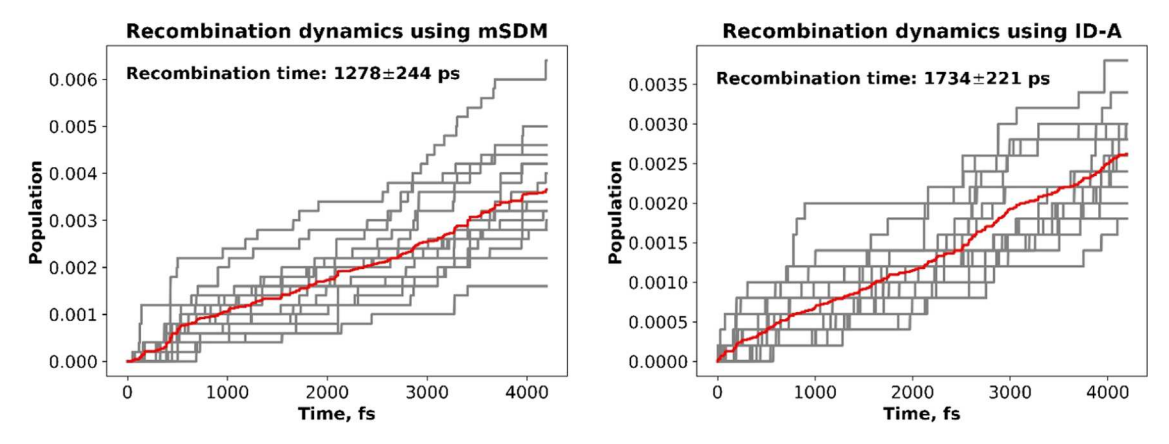


Figure 6. Population of the ground state for the stochastic dynamics initiated from the first excited state using the mSDM and ID-A approaches. "Population" refers to the population of the ground state.

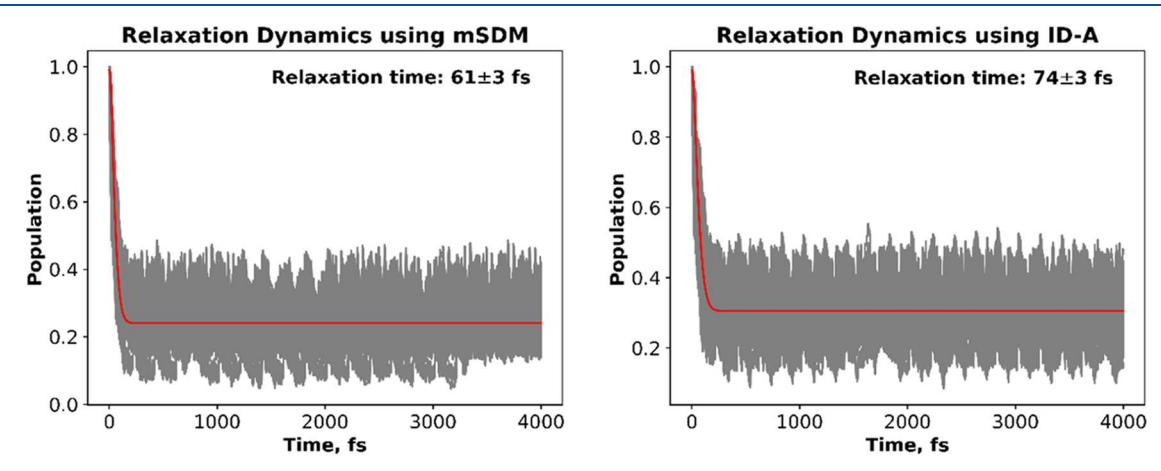


Figure 7. Relaxation dynamics using mSDM and ID-A from the 50th excited state to the first excited state using all MD steps with R² larger than 0.2. The axis label "population" refers to the population of the 50th excited state.

GS-to-excited state couplings, the NACs among excited states are much larger. For example, the trajectory-averaged NAC magnitudes between the first excited state and the second, 10th, 20th, 30th, 40th, and 50th excited states are 24.73, 15.74, 12.18, 10.09, 9.33, and 8.42 meV respectively. Their larger magnitude can be attributed to the many-body effects and the near degeneracy of the Fe 3d states that form the conduction band.

III.III. Recombination Lifetimes. The results for the recombination time from the first excited states using mSDM and ID-A approaches are illustrated in Figure 6. It can be observed from the left panel of Figure 6, that for the mSDM approach, the recombination time for the dynamics initiated from the first excited state is found to be around ~1278 ps. When the simulations are initiated from other excited states (10th, 20th, ..., 50th), the recombination time is within the range of 1100–1300 ps, with no discernible pattern in the recombination time with respect to selection of the initial state. The results for the ID-A approach are like those of the mSDM, with a range of 1500–1800 ps and no specific pattern in relation to the initial excitation. The recombination dynamics initiated from the first excited state using ID-A is illustrated in the right panel of Figure 6.

We note that during the stochastic dynamics, excitons may hop not only to lower-lying excited states but also to higher ones. The large NAC values among excited states and small NAC values between the excited states and the ground state are consistent with the observed long recombination (ground state recovery) times. ^{45,62} Direct recombination has a very small probability, and large NAC values between excited states facilitate rapid interconversion between these states and delay recombination to the ground state.

III.IV. Relaxation Lifetime. The relaxation dynamics from the 50th excited state to a narrow energy range near the lowest excited state is illustrated in Figure 7 using the mSDM and ID-A approaches. A fitting criterion of R-squared values being larger than 0.2 was applied. However, various R-squared values were explored to calculate the relaxation time, as elaborated further in Table S1 in the SI file. To determine the higher-lying exciton relaxation lifetime using the mSDM and the ID-A approaches, we note that the 50th excited state has an average energy of \sim 1.96 eV with a range of \sim 1.88 to \sim 2.05 eV with an initial excitation energy of \sim 0.2 eV above the first excited state. The first excited state has an average energy of \sim 1.75 eV and a range of energy $\sim 1.43-1.92$ eV above the ground state. The relaxation from excited states # 50, 40, 30, 20, and 10 were also calculated using the mSDM and ID-A approaches. The data are given in Table 1 and discussed below.

Recall that the nature of the excited state spectrum with very small spacing between excited states within 0.2 eV of the lowest excited state presents challenges in the convergence of relaxation. As indicated earlier, this led us to define an energy window of 0.03 eV above the lowest excited state within which relaxation is declared "achieved".

Table 1. Relaxation times Using mSDM and ID-A with $R^2 = 0.2$ and Fittings of all MD Steps, Starting from Different Excited States down to Low Excited States within an Energy Window = 0.03 eV from the Lowest Excited State

initial excited state in relaxation	average excitation energy (eV)	maximum excitation energy (eV)	minimum excitation energy (eV)	relaxation time (fs) using mSDM	relaxation time (fs) using ID-A
50	1.96	2.05	1.88	61 ± 3	74 ± 3
40	1.95	2.03	1.85	62 ± 2	74 ± 3
30	1.92	2.02	1.82	56 ± 2	72 ± 3
20	1.90	2.00	1.78	58 ± 3	67 ± 3
10	1.85	1.98	1.69	57 ± 3	65 ± 4

Relaxation times for different initial excited states from mSDM and ID-A simulations in Table 1 exhibit no drastic changes in the magnitude of the order of $\sim\!60-70$ fs; this implies a rapid relaxation process. Notably, the ID-A values are slightly larger, approximately 20%, than the corresponding mSDM values. Furthermore, it is observed that the relaxation times for lower excited states are smaller compared to those for higher excited states.

As discussed in the Introduction, reported experiment-derived lifetimes are on the order of hundreds of picoseconds for photoexcited carriers in hematite. However, the experimental studies used an initial excitation at 400 nm, which is equivalent to 3.1 eV, to generate higher-lying carriers. 18,65 This is significantly larger than the 1.96 eV used in the present computational study. The latter value is consistent with the visible light range that is targeted by PECs. However, the visible light range of interest in the context of photoelectrochemical cells is $\sim\!\!470$ to 750 nm, or 2.64 to 1.65 eV. 65 Accordingly, the range of $\sim\!\!1.88\!-\!2.05$ eV considered here is more closely connected to the situation in PECs.

III.V. The First Excited State Energy Surface. In this section, we aim to establish that the shape of the potential energy surface for the first excited state is as depicted in Figure 1. We aim to assert whether, upon vertical excitation, the first excited state resides or not in a quasi-bound metastable state corresponding to a local energy minimum in the region of the GS structure. Our results point to the excited surface having the shape of a valley that leads to the Exc-3 structure. Our assertion that the Exc-3 structure is a local energy minimum will be shown by the vibrational analysis of the Exc-3 structure.

Figure 8 shows the energy profile of the 1st-Ex state relative to the energy of the 1st-Ex state at the GS structure along the *steepest descent path* upon vertical excitation at the GS structure using the DFT+U(Fe,O) plus TD-DFT level of theory in

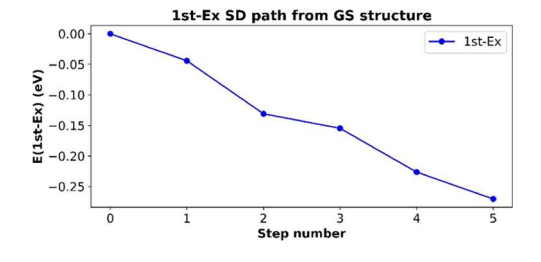


Figure 8. Energy (eV) of the 1st-Ex state along the steepest descent path starting from the GS structure. Only the first five steps along the steeped descent path are shown, with the system reaching the energy of ~ -0.27 eV. Continuation of the steepest descent path would lead to the minimum energy structure at ~ -0.32 eV.

connection with a $2 \times 2 \times 1$ supercell (the absolute energies of the GS and 1st-Ex state in atomic unit are given in Table S2 of the SI file.) The first five steepest descent steps are downhill with the total energy going down by ~ 0.27 eV. This is a substantial fraction of the relaxation energy at the local minimum structure Exc-3. This result strongly validates the shape of the 1st-Ex energy surface depicted in Figure 1.

Another one-dimensional (1D) cut in the potential energy surface of the 1st-Ex is the linearized pathway that morphs the GS structure and the Exc-3 structure, parametrized in eq 7 as follows

$$X(\lambda) = (1 - \lambda)X(GS) + \lambda X(Exc-3)\lambda = 0.0 \text{ to } 1.0$$
 (7)

where $X(\lambda)$ is the vector made up of the 3N Cartesian coordinates of the N atoms in the supercell, X(GS) and X(Exc-3) are vectors of the 3N Cartesian coordinates of the GS and Exc-3 structures, respectively. This morphing pathway is often adopted to parametrize the energy profile for the two state model of polaron hopping in the Marcus/Holstein formalism. ^{66–68} If the 1st-Ex were in a local energy minimum upon vertical excitation, then the "Marcus" profile would be expected to exhibit a double well shape, but this is not the case. The absolute energy along the Marcus path decreases from the initial structure GS to the final structure Exc-3, as seen in Figure 9 (shown in the diagram is the absolute energy relative

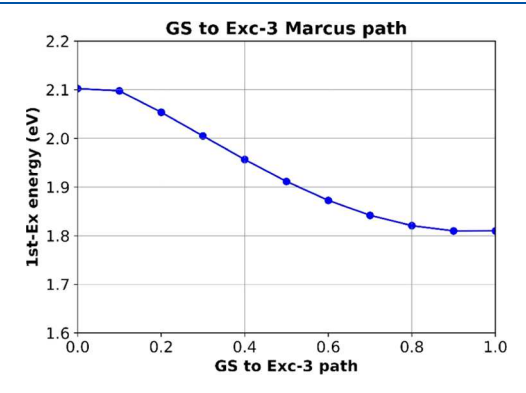


Figure 9. 1st-Ex energy along the linearized "Marcus" pathway morphing the GS structure and the Exc-3 structure.

to the energy of the GS at the GS structure) and as given in Table S3 of SI file. Thus, the Marcus path is a one-dimensional cut of the 3N energy surface that exhibits a downhill-only behavior. The modified vibration analysis based on the "Marcus" direction vector complemented with a Gram-Schmidt set of displacement vectors (see Section II above) and carried out for the 1st-Ex state at the Exc-3 structure yielded a 1D frequency along the Marcus direction of ~345.7 cm⁻¹. When accounting for the coupling to the 3N-1 dimension, several normal modes have rather large contributions from the Marcus direction, with the mode at ~230.5 cm⁻¹ having the largest one. Alternately, using the gradient vector and direction for the 1st-Ex state at the GS structure as the 1D direction in the modified vibration analysis, we get the curvature of the 1st-Ex energy surface along that direction to be ~525 cm⁻¹. When accounting for the couplings to the perpendicular directional modes, there are again several modes with rather large components along the gradient direction, and the mode with the largest component has the frequency of \sim 645 cm⁻¹. The positiveness of the above curvatures (frequencies) provides strong support that the 1st-Ex energy

surface is one of a single well evolving from the GS structure to the Exc-3 structure. All in all, we believe that these three pieces of evidence support the qualitative diagram of Figure 1.

III.VI. -Exciton Hopping. Figure 1 above depicts the relative stability of the Exc-3, Exc-5, Exc-7, and Exc-9 as computed in Paper I. As the separation between the electron state site and the hole state site increases, the relative energies of these structures (all local minima on the potential energy surface of the 1st-Ex state) decreases and becomes very small. The sites feel less and less the presence of the other sites. Conceptually we can think of the electron state site remaining at the same "site" and the hole state site hopping from one basal plane (3, or 5, or 7 away) to another basal plane (5, or 7, or 9 away). The process is very similar to the traditional polarons hopping process described by Marcus⁶⁶ and Emin/Holstein. 67,68

We used "Marcus" pathways analogous to eq 8 to define the hopping pathways:

$$X(\lambda) = (1 - \lambda)X(Exc-i) + \lambda X(Exc-j)\lambda = 0.0 \text{ to } 1.0$$
 (8)

where "Exc-i" and "Exc-j" denote the excitons structure Exc-3, Exc-5, Exc-7, Exc-9. The energy profiles for the combined pathways from GS to Exc-9 are displayed in Figure 10. The

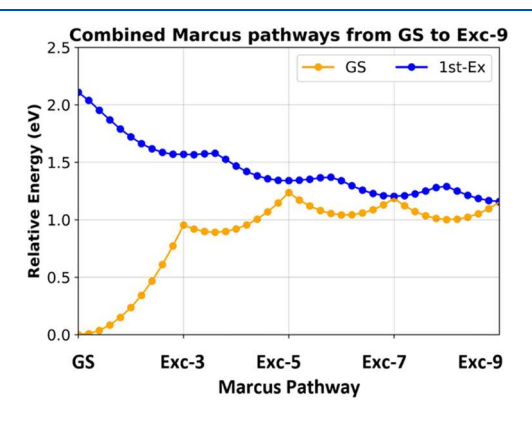


Figure 10. Combined energy profile of the GS and 1st-Ex states along the four "Marcus pathways", GS to Exc-3, Exc-3 to Exc-5, Exc-5 to Exc-7, and Exc-7 to Exc-9. The hopping separation process occurs on the blue energy profile. Pathway "GS to Exc-3" shows no barrier, the other three pathways show an increasing energy barrier that correlates with the smaller exothermicity of any pathway over the previous. See text for discussion.

data is given in Table S4 of the SI. We display the GS energy relative to the energy of the GS structure and the 1st-Ex state energy relative to the GS energy at the GS structure. The GS energy along the profile is in fact the "distortion" energy for the GS and its overall shape is broadly increasing up to the GS distortion energy of separated electron-hole polarons. The complete curve is comprised of four Marcus pathways. The deeps in GS energy when going from Exc-3 to Exc-5 to Exc-7 and to Exc-9 arises from each pathway morphing the hole site from Exc-i to Exc-j. At intermediate points along the pathways, the initial hole site disappears while reappearing at the final hole site, giving rise to a lesser distortion energy of the GS state. For the 1st-Ex excited state energy profile, the three hops, Exc-3 to Exc-5 to Exc-7 to Exc-9 exhibit an energy barrier, a small one (~0.01 eV) for the Exc-3 to Exc-5 hop, a little larger one (~0.03 eV) for the Exc-5 to Exc-7 hop, and the largest one (\sim 0.09 eV) for the Exc-7 to Exc-9 hop. The trend is consistent with the exothermicity of these hops being increasingly smaller and the barrier being increasingly larger in accord with the Bell- Evans–Polanyi principle. ^{69,70}

III.VII. Phonon Analyses of GS and Exc-3. For the GS state at the GS structure, calculated harmonic frequencies and IR intensities are shown in Figure 11. The calculated

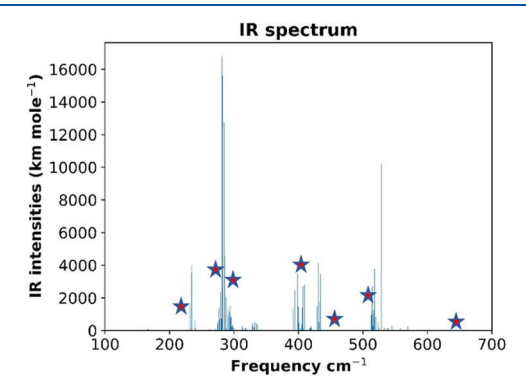


Figure 11. IR spectrum of the $\mathrm{Fe_2O_3}$ ground state at the $2\times2\times1$ GS optimized structure. The red stars indicate approximately frequencies that have been identified experimentally. See Table 2 and references therein.

frequencies range between ~120 cm⁻¹ and ~667 cm⁻¹. Experimental IR assignments by Onari et al.⁷¹ and Serna et al.⁷² and IR and Raman assignments by Jubb et al.⁷³ are gathered in Table 2 and marked with stars in Figure 11. The

Table 2. IR Active Transverse Optical (TO) and Longitudinal Optical (LO) and Raman Active Phonon frequencies (cm⁻¹) for Fe₂O₃ (GS) from (Onari et al. (ref 71.) Serna et al. (ref 72.), and Jubb et al. (ref 73))

IR	TO	A2u: 299, 526	Eu: 227, 286 , 437, 524
	LO	A2u: 414, 662	Eu: 230, 368, 494, 662
		A2u: 385, 526	Eu: 436-459, 526
Raman		A1g: 229, 500	Eg: 249, 295 , 302, 414, 615

calculated high IR intensity mode frequency~ 529 cm⁻¹ matches well the experimental peak at ~526 cm⁻¹. Very high IR intensity peaks are calculated at ~281 to 285 cm⁻¹ and appear to match well observed peaks. The medium IR intensity peaks at ~431 to 434 cm⁻¹ appear to match the experimental IR peaks in the range ~436 to 459 cm⁻¹. Calculated peaks above ~550 cm⁻¹ are predicted to have low IR intensities. The calculations do not yield Raman intensities, albeit we note the calculated highest frequency is at ~667 cm⁻¹, possibly matching an observed Raman peak at ~660 cm⁻¹. Overall, it can be said that the calculated frequencies are in good accord with the observed IR and Raman peaks.

For the 1st-Ex state at the Exc-3 structure, the range of calculated frequencies at the Exc-3 $2 \times 2 \times 1$ optimized geometry is from ~92 to 672 cm^{-1} . This is comparable to the range of ~120 to 667 cm^{-1} for the ground state at the GS optimized geometry. A heatmap comparing the two sets of frequencies is shown in Figure S3 of the Supporting Information (SI). The heatmap depicts the position of the frequencies. It illustrates that the frequency ranges are very similar. However, a few phonon frequencies of the 1st-Ex state fall within gaps where no GS phonon frequencies are present. Assigning these additional phonon frequencies, relative to the ground state at the GS optimized geometry, to the HOMO

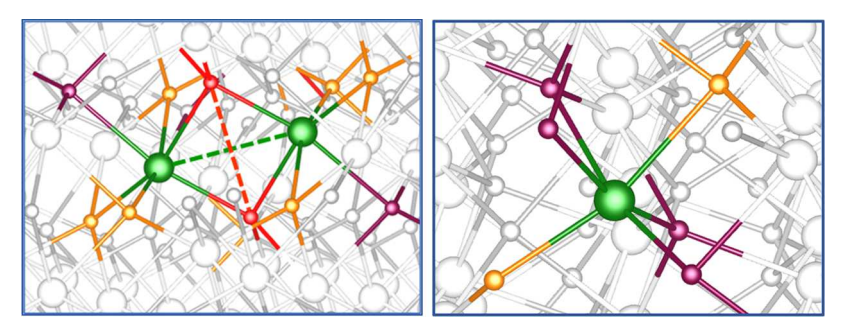


Figure 12. Excised 12-cluster and 7-cluster for the LUMO electron site (left panel) and the HOMO hole site (right panel) of the excitonic Exc-3 structure. Fe atoms are in green. The O atoms with significant Fe-O changes are in purple, and those with smallest Fe-O changes are in yellow orange. The O atoms of the shared edge are in red orange. The smaller excised clusters are those in green Fe and purple O atoms denoted 4-cluster and 5-cluster. The GVSA analysis uses the 4-cluster and 5-cluster to identify the signature frequencies of the exciton structure Exc-3. The green dash line suggests the Fe-Fe bond in the LUMO site, the red orange dash line links the edge-sharing O atoms of the LUMO site.

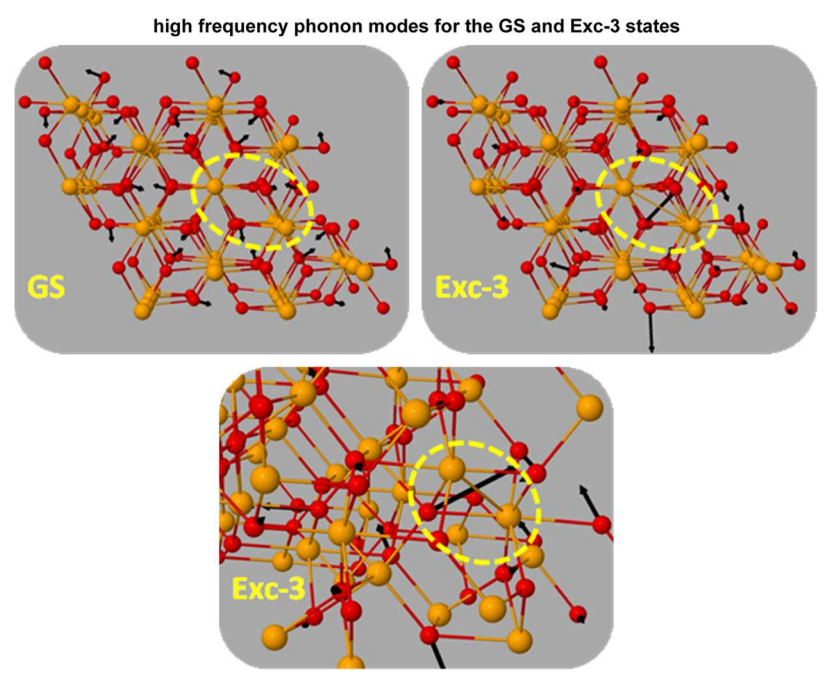


Figure 13. Highest frequency modes (\sim 667 cm⁻¹) of the GS state at the GS optimized structure (top left panel) and (\sim 672 cm⁻¹) of 1st-Ex state at the optimized exciton structure Exc-3 (top right panel). The bottom panel is a close-up view of the mode in the top right panel. The views are along the c direction of the 2 × 2 × 1 supercell. The black vectors associated with the atoms are the mass-weighted Cartesian displacements in the modes. The dotted line circles highlight the location of the electron state (LUMO) site of the exciton with the shorter Fe—Fe distance in Exc-3. The GS mode exhibits notable symmetries among the displacements across the supercell. In contrasts, the Exc-3 mode shows strong localization of the atomic displacements associated with the lattice distortions of the LUMO site. It is notable that this is the highest frequency mode for Exc-3, we surmise that this feature will remain in the Exc-5, Exc-9, and beyond as the electron/hole polarons separate.

hole site and the LUMO electron site of the excitonic structure is quite challenging.

The identification of modes that are unique to the polaronic lattice distortions of the electron state and hole state of the Exc-3 excitonic structure can be conveniently carried out through the GSVA analysis mentioned in Section II above. Excised 12-cluster and 7-cluster associated with the LUMO and HOMO sites are highlighted in Figure 12 with the relevant Fe atoms in green and the O atoms in orange, red orange, and purple. The associated Fe—O bonds are given in Table S5 in the SI file for the GS structure and the Exc-3 structure. The purple atoms stand out as having the largest change between GS and Exc-3, so that the local assignment could be made from a 4-cluster for the LUMO site and a 5-cluster for the HOMO site involving the Fe green atoms and the purple O atoms.

In the 4-cluster model of the LUMO site (electron state) we recognize a symmetric stretch of the two Fe–O bonds with a frequency of \sim 420 cm⁻¹, an asymmetric stretch of those bonds with a frequency of \sim 334 cm⁻¹, and a Fe–Fe stretch with a frequency of \sim 189 cm⁻¹ shown in SI. With the GVSA analysis, we can identify the full system Exc-3 modes that most closely resemble these three modes. They have frequencies of \sim 431, \sim 473, and \sim 163 cm⁻¹. The frequency shifts between the subsystem modes and the full systems modes are due to the coupling to the "other" modes in the full system. Four frequencies in the 5-cluster of the HOMO site (hole state) that can be assigned to Fe–O stretching modes are at \sim 230, 320, 420, and 479 cm⁻¹ that can be mapped to full system modes with frequencies at \sim 339, 414, 516, 576 cm⁻¹.

A technical limitation encountered with the phonon calculation with CP2K here is the absence of a determination

of dipole and polarizability derivatives (with respect to the nuclear coordinates) for TD-DFT excited states and therefore the absence of IR and Raman intensities. Because of that, it is unclear whether these modes assigned to the polaronic sites can be detected or not. Perhaps the asymmetric modes mentioned above might be detectable in IR and the symmetric modes in Raman.

Taking a more global view, Figure 13 displays the highest frequency mode at ~667 cm⁻¹ for the GS system at the GS structure and the one at \sim 671 cm⁻¹ for the 1st-Ex state at the Exc-3 structure with its lattice distortions. There is a striking difference between the GS mode (top left panel of Figure 13) and the Exc-3 mode (top right panel and bottom panel of Figure 13). The atomic displacements in the GS mode exhibit symmetries among the displacements, not surprisingly given the structural symmetry within the GS supercell. In contrast, the atomic displacements in the highest frequency mode of the Exc-3 state are notably associated with the LUMO site of the electron state of the exciton. The largest displacement is associated with one of the edge-sharing O atoms in the octahedron pair that forms the LUMO site. With the increase in electron density shared between the two Fe atoms that induces a Fe-Fe distance shortening, the same electron density pushes the two edge-sharing O atoms away (see Table S5 in SI) with the O-O distance. The edge-sharing atoms form shorter and stronger bonds with one of the two other Fe atoms to which they are bound. The displacement arrow is a clear manifestation of this effect. We note that this mode is the highest frequency mode in Exc-3. It is a signature of the LUMO site. In the context of the exciton separation along the Exc-3, Exc-5, Exc-7, Exc-9, and beyond depicted in Figure 1, we surmise that this vibrational feature will remain given the similarity between all these structures and may become a signature of separated electron/hole polarons. This mode and frequency could be associated with the peak observed at ~641 cm⁻¹ over a long time scale by Šuligoj et al.²² upon irradiation.

IV. CONCLUSIONS

This study constitutes the second part of our computational investigation of the electronic structure and excited states dynamics of excitons in hematite. Employing the NA-MD methodology coupled to the many-body (TD-DFT) description of excited states, we computed relaxation and ground-state recovery (recombination) times. The theories that accounted for decoherence, yielded fast relaxation times of the order of ~60 to 75 fs. Recombination times are much longer, calculated to be between \sim 1.1 and 1.8 ns. These times are consistent with experimental observations. The fast relaxation times suggest that the higher-lying excitons quickly relax to the lower-energy states. We identified several metastable electronic structure states on the first excited state potential energy surface that have the character of electron-hole pair states with increasing electron-hole separation, namely Exc-3, Exc-5, Exc-7, Exc-9. These states are involved in the process of exciton separation into separated electron and hole polarons by hopping. We determined the phonon spectrum of the ground state of hematite and the exciton Exc-3 state. Given the similarities of the electron LUMO and hole HOMO sites among the series of metastable excitonic structures, we surmise that the vibrational features will remain for separated electron and hole polarons. An electron polaron vibrational peak calculated at ~672 cm is a candidate for assignment to the postirradiation peak observed in a long-time scale at \sim 641 cm⁻¹.

Beyond the specific findings for hematite, this two-part investigation represents a successful application of the combined TD-DFT plus NA-MD approach to obtain an accurate atomistic-scale characterization of the electronic structure and dynamics of electron-hole pairs in transition metal-based semiconductors. The approach allows quantitative comparison with detailed atomic-level experimental structural data about excitons that are becoming available for this type of materials. Noting that the success of TD-DFT in the present case is for high spin d5 cations Fe(III)-containing materials, investigating d0-type and d10-type semiconductors would be specially instructive about the power of the electronic structure approach in handling distinctly different materials. Another area of great interest includes the application of the TD-DFT plus NA-MD protocol used here to solid-liquid interfaces. Electric fields resulting from the surface termination and the liquid phase are believed to be responsible for hole trapping and charge carrier recombination. Studies like the present one and others are starting to contribute to the growing body of electronic structure information needed to develop new semiconductor materials with enhanced charge carrier generation, transport, and redox performance.

ASSOCIATED CONTENT

Supporting Information

The Supporting Information is available free of charge at https://pubs.acs.org/doi/10.1021/acs.jpcc.4c03247.

Additional details about the relaxation time calculation, the energy profile for the 1st-Ex state, the "Marcus" pathways, the vibrational analyses, and the molecular dynamics simulation data (PDF)

AUTHOR INFORMATION

Corresponding Author

Michel Dupuis — Department of Chemical and Biological Engineering, University at Buffalo, Buffalo, New York 14260, United States; Computation and Data-enabled Science and Engineering Program, University at Buffalo, Buffalo, New York 14260, United States; ◎ orcid.org/0000-0003-4799-3364; Phone: (716) 645-9062; Email: mdupuis2@buffalo.edu

Authors

Lili Rassouli — Department of Chemical and Biological Engineering, University at Buffalo, Buffalo, New York 14260, United States; © orcid.org/0000-0003-0993-4435

Mohammad Shakiba — Department of Chemistry, University at Buffalo, Buffalo, New York 14260, United States

Alexey V. Akimov — Department of Chemistry, University at Buffalo, Buffalo, New York 14260, United States;
orcid.org/0000-0002-7815-3731

Xuyan Ma – Department of Chemical and Biological Engineering, University at Buffalo, Buffalo, New York 14260, United States

Complete contact information is available at: https://pubs.acs.org/10.1021/acs.jpcc.4c03247

Notes

The authors declare no competing financial interest.

ACKNOWLEDGMENTS

L.R., X.M., and M.D. acknowledge support from the U.S. Department of Energy, Office of Science, Office of Basic Energy Sciences, under Award Number DE-SC0019086. M.D. acknowledges support from the National Science Foundation (NSF) under grant CHE-2052862. A.V.A. acknowledges the financial support of the National Science Foundation (Grant OAC-NSF1931366). Support for the computations is provided by the Center for Computational Research at the University at Buffalo.

REFERENCES

- (1) Grätzel, M. Photoelectrochemical Cells. *Nature* **2001**, *414*, 338–344.
- (2) Segev, G.; Kibsgaard, J.; Hahn, C.; Xu, Z. J.; Deutsch, T. G.; Xiang, C.; Zhang, J. Z.; Hammarström, L.; Nocera, D. G.; Weber, A. Z.; et al. The 2022 Solar Fuels Roadmap. J. Phys. D: Appl. Phys. 2022, 55, No. 323003.
- (3) Yang, J.; Wang, D.; Han, H.; Li, C. Roles of Cocatalysts in Photocatalysis and Photoelectrocatalysis. *Acc. Chem. Res.* **2013**, *46*, 1900–1909.
- (4) Gong, J. L.; Li, C.; Wasielewski, M. R. Advances in Solar Energy Conversion. *Chem. Soc. Rev.* **2019**, 48, 1862–1864.
- (5) Han, H.; Li, C. Photocatalysis in Solar Fuel Production. *Natl. Sci. Rev.* **2015**, *2*, 145–147.
- (6) Sivula, K.; Van De Krol, R. Semiconducting Materials for Photoelectrochemical Energy Conversion. *Nat. Rev. Mater.* **2016**, *1*, No. 15010.
- (7) Sivula, K.; Le Formal, F.; Grätzel, M. Solar Water Splitting: Progress Using Hematite (α -Fe₂O₃) Photoelectrodes. *ChemSusChem* **2011**, *4*, 432–449.
- (8) Zandi, O.; Hamann, T. W. The Potential Versus Current State of Water Splitting with Hematite. *Phys. Chem. Chem. Phys.* **2015**, *17*, 22485–22503.
- (9) Biswas, S.; Husek, J.; Londo, S.; Baker, L. R. Highly Localized Charge Transfer Excitons in Metal Oxide Semiconductors. *Nano Lett.* **2018**, *18*, 1228–1233.
- (10) Rassouli, L.; Dupuis, M. Electronic Structure of Excitons in Hematite Fe₂O₃. *J. Phys. Chem. C* **2024**, 128, 743–758.
- (11) Corby, S.; Rao, R. R.; Steier, L.; Durrant, J. R. The Kinetics of Metal Oxide Photoanodes from Charge Generation to Catalysis. *Nat. Rev. Mater.* **2021**, *6*, 1136–1155.
- (12) Marschall, R. Semiconductor Composites: Strategies for Enhancing Charge Carrier Separation to Improve Photocatalytic Activity. *Adv. Funct. Mater.* **2014**, *24*, 2421–2440.
- (13) Uemura, Y.; Ismail, A. S. M.; Park, S. H.; Kwon, S.; Kim, M.; Elnaggar, H.; Frati, F.; Wadati, H.; Hirata, Y.; Zhang, Y.; et al. Hole Dynamics in Photoexcited Hematite Studied with Femtosecond Oxygen K-Edge X-Ray Absorption Spectroscopy. *J. Phys. Chem. Lett.* **2022**, *13*, 4207–4214.
- (14) Ellis, D. S.; Wang, R. P.; Wong, D.; Cooper, J. K.; Schulz, C.; Chuang, Y. D.; Piekner, Y.; Grave, D. A.; Schleuning, M.; Friedrich, D.; et al. Electronic Excitations of α -Fe₂O₃ Heteroepitaxial Films Measured by Resonant Inelastic X-Ray Scattering at the Fe *L* Edge. *Phys. Rev. B* **2022**, *105*, No. 075101.
- (15) Biswas, S.; Wallentine, S.; Bandaranayake, S.; Baker, L. R. Controlling Polaron Formation at Hematite Surfaces by Molecular Functionalization Probed by XUV Reflection-Absorption Spectroscopy. *J. Chem. Phys.* **2019**, *151*, No. 104701.
- (16) Carneiro, L. M.; Cushing, S. K.; Liu, C.; Su, Y. D.; Yang, P. D.; Alivisatos, A. P.; Leone, S. R. Excitation-Wavelength-Dependent Small Polaron Trapping of Photoexcited Carriers in α -Fe₂O₃. *Nat. Mater.* **2017**, *16*, 819–826.
- (17) Biswas, S.; Husek, J.; Baker, L. R. Elucidating Ultrafast Electron Dynamics at Surfaces Using Extreme Ultraviolet (XUV) Reflection—Absorption Spectroscopy. *Chem. Commun.* **2018**, *54*, 4216–4230.

- (18) Husek, J.; Cirri, A.; Biswas, S.; Baker, L. R. Surface Electron Dynamics in Hematite (α -Fe₂O₃): Correlation between Ultrafast Surface Electron Trapping and Small Polaron Formation. *Chem. Sci.* **2017**, *8*, 8170–8178.
- (19) Ismail, A. S. M.; Uemura, Y.; Park, S. H.; Kwon, S.; Kim, M.; Elnaggar, H.; Frati, F.; Niwa, Y.; Wadati, H.; Hirata, Y.; et al. Direct Observation of the Electronic States of Photoexcited Hematite with Ultrafast 2p3d X-Ray Absorption Spectroscopy and Resonant Inelastic X-Ray Scattering. *Phys. Chem. Chem. Phys.* **2020**, 22, 2685–2692.
- (20) Vura-Weis, J.; Jiang, C. M.; Liu, C.; Gao, H. W.; Lucas, J. M.; de Groot, F. M. F.; Yang, P. D.; Alivisatos, A. P.; Leone, S. R. Femtosecond M-2,M-3-Edge Spectroscopy of Transition-Metal Oxides: Photoinduced Oxidation State Change in α -Fe₂O₃. *J. Phys. Chem. Lett.* **2013**, *4*, 3667–3671.
- (21) Joly, A. G.; Williams, J. R.; Chambers, S. A.; Xiong, G.; Hess, W. P.; Laman, D. M. Carrier Dynamics in α -Fe₂O₃ (0001) Thin Films and Single Crystals Probed by Femtosecond Transient Absorption and Reflectivity. *J. Appl. Phys.* **2006**, *99*, No. 053521.
- (22) Šuligoj, A.; Grinberg, D.; Paz, Y. Post-Excitation Transient IR Phenomena in α -Fe₂O₃ Films. *J. Phys. Chem. C* **2021**, *125*, 28013–28024.
- (23) Piccinin, S. The Band Structure and Optical Absorption of Hematite (α -Fe₂O₃): A First-Principles GW-BSE Study. *Phys. Chem. Phys.* **2019**, 21, 2957–2967.
- (24) Snir, N.; Toroker, M. C. The Operando Optical Spectrum of Hematite During Water Splitting through a GW–BSE Calculation. *J. Chem. Theory Comput.* **2020**, *16*, 4857–4864.
- (25) Ahart, C. S.; Blumberger, J.; Rosso, K. M. Polaronic Structure of Excess Electrons and Holes for a Series of Bulk Iron Oxides. *Phys. Chem. Chem. Phys.* **2020**, *22*, 10699–10709.
- (26) Shelton, J. L.; Knowles, K. E. Thermally Activated Optical Absorption into Polaronic States in Hematite. *J. Phys. Chem. Lett.* **2021**, *12*, 3343–3351.
- (27) Shelton, J. L.; Knowles, K. E. Polaronic Optical Transitions in Hematite (α -Fe₂O₃) Revealed by First-Principles Electron—Phonon Coupling. *J. Chem. Phys.* **2022**, *157*, No. 174703.
- (28) Cheng, C.; Zhu, Y.; Zhou, Z.; Long, R.; Fang, W. H. Photoinduced Small Electron Polarons Generation and Recombination in Hematite. *Npj Comput. Mater.* **2022**, *8*, No. 148.
- (29) Klein, I. M.; Liu, H. Z.; Nimlos, D.; Krotz, A.; Cushing, S. K. Ab Initio Prediction of Excited-State and Polaron Effects in Transient XUV Measurements of α -Fe₂O₃. *J. Am. Chem. Soc.* **2022**, *144*, 12834–12841.
- (30) Tao, Y.; Tian, C.; Verma, N.; Zou, W.; Wang, C.; Cremer, D.; Kraka, E. Recovering Intrinsic Fragmental Vibrations Using the Generalized Subsystem Vibrational Analysis. *J. Chem. Theory Comput.* **2018**, *14*, 2558–2569.
- (31) Liechtenstein, A. I.; Anisimov, V. I.; Zaanen, J. Density-Functional Theory and Strong-Interactions Orbital Ordering in Mott-Hubbard Insulators. *Phys. Rev. B* **1995**, *52*, R5467–R5470.
- (32) Anisimov, V. I.; Zaanen, J.; Andersen, O. K. Band Theory and Mott Insulators: Hubbard U Instead of Stoner I. *Phys. Rev. B* **1991**, 44, 943–954.
- (33) Perdew, J. P.; Burke, K.; Ernzerhof, M. Generalized Gradient Approximation Made Simple. *Phys. Rev. Lett.* **1996**, *77*, 3865–3868.
- (34) Kohn, W.; Sham, L. J. Self-Consistent Equations Including Exchange and Correlation Effects. *Phys. Rev.* **1965**, *140*, No. 1133.
- (35) Hubbard, J. The Description of Collective Motions in Terms of Many-Body Perturbation Theory. II. The Correlation Energy of a Free-Electron Gas. *Proc. R. Soc. A* **1958**, 243, 336–352.
- (36) Kumari, S.; Singh, A. P.; Sonal; Deva, D.; Shrivastav, R.; Dass, S.; Satsangi, V. R. Spray Pyrolytically Deposited Nanoporous Ti⁴⁺ Doped Hematite Thin Films for Efficient Photoelectrochemical Splitting of Water. *Int. J. Hydrogen Energy* **2010**, *35*, 3985–3990.
- (37) VandeVondele, J.; Hutter, J. Gaussian Basis Sets for Accurate Calculations on Molecular Systems in Gas and Condensed Phases. *J. Chem. Phys.* **2007**, *127*, No. 114105.

- (38) Goedecker, S.; Teter, M.; Hutter, J. Separable Dual-Space Gaussian Pseudopotentials. *Phys. Rev. B* **1996**, *54*, 1703–1710.
- (39) Maslen, E. N.; Streltsov, V. A.; Streltsova, N. R.; Ishizawa, N. Synchrotron X-Ray Study of the Electron Density in α -Fe₂O₃. *Acta Crystallogr., Sect. B: Struct. Sci.* **1994**, *50*, 435–441.
- (40) Finger, L. W.; Hazen, R. M. Crystal Structure an Isothermal Compression of Fe_2O_3 , Cr_2O_3 , and V_2O_3 to 50 Kbars. *J. Appl. Phys.* **1980**, *51*, 5362–5367.
- (41) Kühne, T. D.; Iannuzzi, M.; Del Ben, M.; Rybkin, V. V.; Seewald, P.; Stein, F.; Laino, T.; Khaliullin, R. Z.; Schutt, O.; Schiffmann, F.; et al. CP2K: An Electronic Structure and Molecular Dynamics Software Package Quickstep: Efficient and Accurate Electronic Structure Calculations. *J. Chem. Phys.* **2020**, *152*, No. 194103.
- (42) Bussi, G.; Donadio, D.; Parrinello, M. Canonical Sampling through Velocity Rescaling. *J. Chem. Phys.* **2007**, *126*, No. 014101.
- (43) Akimov, A. V. Libra: An Open-Source "Methodology Discovery" Library for Quantum and Classical Dynamics Simulations. *J. Comput. Chem.* **2016**, *37*, 1626–1649.
- (44) Shakiba, M.; Smith, B.; Li, W.; Dutra, M.; Jain, A.; Sun, X.; Garashchuk, S.; Akimov, A. Libra: A Modular Software Library for Quantum Nonadiabatic Dynamics. *Software Impacts* **2022**, *14*, No. 100445.
- (45) Smith, B.; Shakiba, M.; Akimov, A. V. Nonadiabatic Dynamics in Si and CdSe Nanoclusters: Many-Body Vs Single-Particle Treatment of Excited States. *J. Chem. Theory Comput.* **2021**, 17, 678–693.
- (46) Shakiba, M.; Stippell, E.; Li, W.; Akimov, A. V. Nonadiabatic Molecular Dynamics with Extended Density Functional Tight-Binding: Application to Nanocrystals and Periodic Solids. *J. Chem. Theory Comput.* **2022**, *18*, 5157–5180.
- (47) Hutter, J.; Iannuzzi, M.; Schiffmann, F.; VandeVondele, J. CP2K: Atomistic Simulations of Condensed Matter Systems. *Wiley Interdiscip. Rev.: Comput. Mol. Sci.* **2014**, *4*, 15–25.
- (48) Tully, J. C. Molecular Dynamics with Electronic Transitions. *J. Chem. Phys.* **1990**, 93, 1061–1071.
- (49) Smith, B.; Akimov, A. V. A Comparative Analysis of Surface Hopping Acceptance and Decoherence Algorithms within the Neglect of Back-Reaction Approximation. *J. Chem. Phys.* **2019**, *151*, No. 124107.
- (50) Granucci, G.; Persico, M. Critical Appraisal of the Fewest Switches Algorithm for Surface Hopping. *J. Chem. Phys.* **2007**, *126*, No. 134114.
- (51) Nelson, T.; Fernandez-Alberti, S.; Roitberg, A. E.; Tretiak, S. Nonadiabatic Excited-State Molecular Dynamics: Treatment of Electronic Decoherence. *J. Chem. Phys.* **2013**, *138*, No. 224111.
- (52) Akimov, A. V. Excited State Dynamics in Monolayer Black Phosphorus Revisited: Accounting for Many- Body Effects. *J. Chem. Phys.* **2021**, *155*, No. 134106.
- (53) Craig, C. F.; Duncan, W. R.; Prezhdo, O. V. Trajectory Surface Hopping in the Time-Dependent Kohn-Sham Approach for Electron-Nuclear Dynamics. *Phys. Rev. Lett.* **2005**, *95*, No. 163001.
- (54) Duncan, W. R.; Craig, C. F.; Prezhdo, O. V. Time-Domain Ab Initio Study of Charge Relaxation and Recombination in Dye-Sensitized TiO₂. *J. Am. Chem. Soc.* **2007**, *129*, 8528–8543.
- (55) Prezhdo, O. V.; Duncan, W. R.; Prezhdo, V. V. Photoinduced Electron Dynamics at the Chromophore–Semiconductor Interface: A Time-Domain Ab Initio Perspective. *Prog. Surf. Sci.* **2009**, *84*, 30–68.
- (56) Hammes-Schiffer, S.; Tully, J. C. Proton Transfer in Solution: Molecular Dynamics with Quantum Transitions. *J. Chem. Phys.* **1994**, 101, 4657–4667.
- (57) Esch, M. P.; Levine, B. G. Decoherence-Corrected Ehrenfest Molecular Dynamics on Many Electronic States. *J. Chem. Phys.* **2020**, 153, No. 114104.
- (58) Esch, M. P.; Levine, B. G. An Accurate, Non-Empirical Method for Incorporating Decoherence into Ehrenfest Dynamics. *J. Chem. Phys.* **2021**, *155*, No. 214101.
- (59) Plasser, F.; Mai, S.; Fumanal, M.; Gindensperger, E.; Daniel, C.; González, L. Strong Influence of Decoherence Corrections and

- Momentum Rescaling in Surface Hopping Dynamics of Transition Metal Complexes. *J. Chem. Theory Comput.* **2019**, *15*, 5031–5045.
- (60) Temen, S.; Akimov, A. V. A Simple Solution to Trivial Crossings: A Stochastic State Tracking Approach. *J. Phys. Chem. Lett.* **2021**, *12*, 850–860.
- (61) Fernandez-Alberti, S.; Roitberg, A. E.; Nelson, T.; Tretiak, S. Identification of Unavoided Crossings in Nonadiabatic Photoexcited Dynamics Involving Multiple Electronic States in Polyatomic Conjugated Molecules. *J. Chem. Phys.* **2012**, *137*, No. 014512.
- (62) Shakiba, M.; Akimov, A. V. Dependence of Electron-Hole Recombination Rates on Charge Carrier Concentration: A Case Study of Nonadiabatic Molecular Dynamics in Graphitic Carbon Nitride Monolayers. *J. Phys. Chem. C* **2023**, *127*, 9083–9096.
- (63) Senanayake, R. D.; Aikens, C. M. Theoretical Investigation of Relaxation Dynamics in the Au₁₈(Sh)₁₄ Thiolate-Protected Gold Nanocluster. *J. Chem. Phys.* **2019**, *151*, No. 094702.
- (64) Akimov, A. V.; Prezhdo, O. V. The PYXAID Program for Non-Adiabatic Molecular Dynamics in Condensed Matter Systems. *J. Chem. Theory Comput.* **2013**, *9*, 4959–4972.
- (65) Sorenson, S.; Driscoll, E.; Haghighat, S.; Dawlaty, J. M. Ultrafast Carrier Dynamics in Hematite Films: The Role of Photoexcited Electrons in the Transient Optical Response. *J. Phys. Chem. C* **2014**, *118*, 23621–23626.
- (66) Marcus, R. A. Electron Transfer Reactions in Chemistry. Theory and Experiment. In *Protein Electron Transfer*; Garland Science, 2020; pp; pp 249–272.
- (67) Emin, D.; Holstein, T. Adiabatic Theory of Hall Mobility of Small Polaron in Hopping Regime. Bull. Am. Phys. Soc. 1968, 13, 464.
- (68) Emin, D.; Holstein, T. Studies of Small-Polaron Motion IV. Adiabatic Theory of the Hall Effect. *Ann. Phys.* **1969**, *53*, 439–520.
- (69) Bell, R. P. The Theory of Reactions Involving Proton Transfers. *Proc. R. Soc. A* **1936**, *154*, 414–429.
- (70) Evans, M. G.; Polanyi, M. Further Considerations on the Thermodynamics of Chemical Equilibria and Reaction Rates. *Trans. Faraday Soc.* **1936**, 32, 1333–1360.
- (71) Onari, S.; Arai, T.; Kudo, K. Infrared Lattice Vibrations and Dielectric Dispersion in α -Fe₂O₃. *Phys. Rev. B* **1977**, *16*, 1717.
- (72) Serna, C. J.; Rendon, J. L.; Iglesias, J. E. Infrared Surface Modes in Corundum-Type Microcrystalline Oxides. *Spectrochim. Acta, Part A* **1982**, *38*, 797–802.
- (73) Jubb, A. M.; Allen, H. C. Vibrational Spectroscopic Characterization of Hematite, Maghemite, and Magnetite Thin Films Produced by Vapor Deposition. *ACS Appl. Mater. Interfaces* **2010**, *2*, 2804–2812.